Micromechanical Simulation of Dynamic Fracture Using the Cohesive Finite Element Method

Jun Zhai

Vikas Tomar

Min Zhou
e-mail: min.zhou@me.gatech.edu

George W. Woodruff School of Mechanical
Engineering,
Georgia Institute of Technology,
Atlanta, GA 30332-0405

Dynamic fracture in two-phase Al_2O_3/TiB_2 ceramic composite microstructures is analyzed explicitly using a cohesive finite element method (CFEM). This framework allows the effects of microstructural heterogeneity, phase morphology, phase distribution, and size scale to be quantified. The analyses consider arbitrary microstructural phase morphologies and entail explicit tracking of crack growth and arbitrary fracture patterns. The approach involves the use of CFEM models that integrate cohesive surfaces along all finite element boundaries as an intrinsic part of the material description. This approach obviates the need for any specific fracture criteria and assigns models the capability of predicting fracture paths and fracture patterns. Calculations are carried out using idealized phase morphologies as well as real phase morphologies in actual material microstructures. Issues analyzed include the influence of microstructural morphology on the fracture behavior, the influence of phase size on fracture resistance, the effect of interphase bonding strength on failure, and the effect of loading rate on fracture.
[DOI: 10.1115/1.1647127]

1 Introduction

Macroscale continuum theories are useful for the prediction of the average response of heterogeneous material systems. To analyze and characterize the effects of underlying microstructural heterogeneity, phase morphology, and phase distribution on material behavior, a framework that recognizes the heterogeneous nature of microscale material microstructures is needed. This framework should allow different length scales in microstructures to be represented. In addition, it should also allow the consideration of different deformation and failure mechanisms. For brittle materials such as glasses, ceramics, and hard composites, the primary failure mechanism is crack and microcrack development. Analyses at the micro and nano-size scales, therefore, require two important considerations. The first one is the explicit representation and account of micro or nano-material structures. The second is the explicit tracking of failure processes in the form of crack/microcrack initiation, growth, and coalescence. The cohesive finite element method (CFEM) is ideally suited for this task as it allows both objectives to be achieved. In this research, we use a CFEM model based on the framework developed by Tomar et al. [1] to carry out characterization and quantification of the failure behavior of two-phase Al_2O_3/TiB_2 ceramic composites with a range of microstructural characteristics.

The CFEM has been used to study a wide variety of issues, including void nucleation (cf. Needleman [2], Tvergaard [3], and Shabrov and Needleman [4]), quasi-static crack growth (cf. Needleman [5–6] and Tvergaard and Hutchinson [7]), dynamic fracture (cf. Xu and Needleman [8], Pandolfi et al. [9], and Ruiz et al. [10]), interfacial fracture (cf. Xu and Needleman [11–12], Siegmund and Needleman [13] and Rosakis et al. [14]), dynamic fragmentation (cf. Camacho and Ortiz [15], Miller et al. [16], and Espinosa et al. [17–18]), dynamic fracture in heterogeneous materials (cf. Zhai and Zhou [19–20]), impact induced delamination in composites (cf. Geubelle and Baylor [21], Minnaar and Zhou [22–23], Espinosa et al. [24], Zou et al. [25] and Xuan et al. [26]), fracture in polymers, ductile tearing, viscoelastic fracture (cf. Rahul-Kumar et al. [27–29] and Roychowdhury et al. [30]),

response of ceramics under multi-axial loading (cf. Zavattieri et al. [31]), simulation of ductile fracture (cf. Scheider and Brocks [32], Gomez and Elices [33] and Yuan and Chen [34]), simulation of crack growth in functionally graded materials (cf. Jin et al. [35]), and crack propagation in quasi-brittle materials like concrete (cf. Carpinteri et al. [36]). These investigations have resulted in better understanding of fracture processes. However, explicit analyses of fracture in heterogeneous material systems have not been carried out extensively. Additionally, the effect of underlying microstructural heterogeneity, phase morphology and phase distribution on dynamic fracture has not been systematically delineated.

There are two approaches to analyze fracture using CFEM when crack path is not known in advance. One is to insert the cohesive elements into the model as fracture develops (cf., e.g., Pandolfi et al. [37], Yu [38], Pandolfi and Ortiz [39]). This approach avoids the issue of cohesive-surface-induced stiffness reduction of the overall model if the traction-separation relation has finite initial stiffness. However, it requires the use of specific fracture initiation criteria that are extrinsic to the overall finite element model. In addition, it is computationally intensive since it involves adaptive meshing to resolve stresses at the tip of an advancing crack. The other approach is to embed cohesive surfaces along all finite element boundaries as part of the physical model (cf., e.g., Xu and Needleman [8], Zhai and Zhou [19–20]). The additional discretization allows the cohesive surfaces to permeate the whole microstructure as an intrinsic part of the material characterization. This form of CFEM obviates the need for fracture initiation and propagation criteria in numerical models. Another perspective is that the fracture criteria are effectively integrated into the model as part of the cohesive relation. This CFEM approach faces the issue of cohesive-surface-induced stiffness reduction of the model if a cohesive relation with a finite initial stiffness is used. However, this issue can be addressed by careful choice of cohesive surface stiffness and finite element size, cf. Tomar et al. [1]. The approach of Xu and Needleman [8] is used in this paper. This choice is based on several considerations. First, it allows us to consider complicated multiple phase microstructures and still keep the analysis intractable. Second, recent nanoscale simulations of interfacial separation have provided evidence supporting the use of cohesive laws with finite initial stiffness, cf. Spearot et al. [40]. Recent asymptotic analyses of mode-I fracture by

---

Table 1 Constitutive parameters for bulk and cohesive surfaces

Compound	Density (kg/m^3)	K_{IC} Mpa$\sqrt{m}$	E (GPa)	ν	T_{max} (GPa)	Δ_{nc}, Δ_{tc} (nm)	Φ_0 (J/m^2)
Al_2O_3	3990	4.0	340	0.23	0.5	100	25
TiB_2	4520	7.2	500	0.12	1.0	100	50
Homogenized Al_2O_3/TiB_2 Composite	4120	3.6	415	0.15	0.65	100	32.5
Al_2O_3/TiB_2 Interface	⋯	⋯	⋯	⋯	0.5	100	25

Fig. 1 Irreversible bilinear cohesive law

Nguyen and Ortiz [45] also suggest the physical basis of traction-separation relations with finite initial stiffness. The initial slope of the cohesive law may have to do with the micro-cracking behavior in solids, cf. Prado and van Mier [43] and Sorensen and Jacobsen [44]. Third, analyses have also shown that cohesive relations with infinite initial stiffness may not allow resolution of certain crack branching behavior, cf. Falk et al. [41]. Recently, it has been found that initially rigid laws may be associated with pathologies in the forms of division by zero (due to the initial infinite slope) and nonconvergence in time (due to discontinuities in the traction-separation relation), cf. Papoulia and Vavasis [42].

For CFEM models with intrinsically embedded cohesive surfaces, a upper bound and a lower bound on element size must be observed, cf. Falk et al. [41] and Klein et al. [46]. Specifically, the element size must be small enough to accurately resolve the stress distribution inside the cohesive zones at crack tips. On the other hand, the cohesive surface contribution to stiffness reduction must be small, imposing a lower bound on the size of the elements. Tomar et al. [1] have carried out detailed analyses of this issue for meshes with ''cross-triangle'' elements arranged in a quadrilateral pattern. Calculations in the current paper are carried out within the limits set therein.

Our analyses here focus on intergranular and intragranular fracture processes in multi-phase microstructures. To characterize the effect of microstructure of a two-phase Al_2O_3/TiB_2 ceramic composite system on its failure resistance, we consider actual micrographs and hypothetical phase morphologies. The bilinear cohesive law used contains an internal state variable to account for irreversible separation processes. To track complex crack/microcrack patterns, arbitrary crack paths, and crack branching, cohesive surfaces are specified along all finite element boundaries as an intrinsic part of the finite element model. All cohesive surfaces serve as potential crack paths in the microstructure, therefore, fracture inside each microstructural phase and along interphase boundaries can be explicitly resolved.

The framework of analysis allows quantitative results from simulations to be used to delineate factors influencing the failure of the materials analyzed. The information obtained is useful for the microstructural engineering of actual materials. The Al_2O_3/TiB_2 ceramic composites used in this research have been developed by Logan [47]. These composites have a wide range of micro and nano phase sizes and phase morphologies. The different microstructures are derived from a range of processing conditions through either self-propagating high temperature synthesis (SHS) or manual mixing (MM) of constituent powders followed by dynamic hot pressing. These materials possess superior wear resistance, high strength, high thermal conductivity, and excellent aesthetic appearance. They have shown a wide range of fracture toughness values some of which are higher than those of both constituents produced separately in bulk. The numerical simulations here will help the identification of microstructural characteristics that significantly influence the behavior of these materials. Although, this analysis concerns one particular material system, the CFEM framework as a tool for explicit microstructural failure analysis is applicable to other material systems as well.
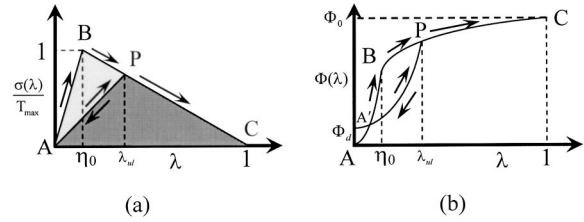
2 Cohesive Model

In the cohesive model used, the traction $\mathbf{T}$ applied on material points P and P' coinciding at and occupying position $\mathbf{x}$ on cohesive surface S_0 in the reference configuration is work-conjugate to surface separation $\boldsymbol{\Delta}$. Reckoned in the reference configuration, the cohesive law is

$$\mathbf{T}(\mathbf{x}) = \mathbf{T}[\boldsymbol{\Delta}(\mathbf{x})] \qquad (1)$$

and the work of separation under this traction at any stage of deformation is (Ortiz and Pandolfi [48]),

$$W_{sep} = \int_{S_0} \int_0^{\Delta} \mathbf{T}(\mathbf{x}) \cdot d\Delta \, dS \qquad (2)$$

Implied here is the assumption that cohesive traction-separation relations are locally determined, i.e., the cohesive traction at one point is fully determined by the separation at the point itself. A review of various types of cohesive laws is given by, e.g., Shet and Chandra [49]. We describe here, the bilinear model used in our analyses.

The bilinear law used can be regarded as a generalized version of those given by Tvergaard and Hutchinson [7] and Ortiz and Pandolfi [48]. However as in Espinosa et al. [24], we have additional parameters to account for the finite initial stiffness of the cohesive surfaces and the irreversibility of separation with damage. This law is derived from a potential Φ which is a function of separation vector $\boldsymbol{\Delta}$ through a state variable defined as $\lambda = \sqrt{(\Delta_n/\Delta_{nc})^2 + (\Delta_t/\Delta_{tc})^2}$. This variable describes the effective instantaneous state of mixed-mode separations. Here, $\Delta_n = \mathbf{n} \cdot \boldsymbol{\Delta}$ and $\Delta_t = \mathbf{t} \cdot \boldsymbol{\Delta}$ denote, respectively, the normal and tangential components of $\boldsymbol{\Delta}$, with $\mathbf{n}$ and $\mathbf{t}$ being unit vectors normal and tangent to S_0 respectively. Δ_{nc} is the critical normal separation at which the cohesive strength of an interface vanishes under conditions of pure normal deformation ($\Delta_t = 0$). Similarly, Δ_{tc} is the critical tangential separation at which the cohesive strength of an interface vanishes under conditions of pure shear deformation ($\Delta_n = 0$). λ tracks instantaneous mixed-mode separations during both loading and unloading. Clearly, $\lambda = 0$ corresponds to $\boldsymbol{\Delta} = \mathbf{0}$ (undeformed state or fully unloaded state) and $\lambda \geq 1$ implies complete separation, i.e., total debonding of the cohesive surface pair.

In order to account for the irreversibility of separations, a parameter $\eta = \max\{\eta_0, \lambda_{ul}\}$ is defined. As illustrated in Fig. 1(a), η_0 is the initial value of η which defines the stiffness of the original undamaged cohesive surface and λ_{ul} is the hitherto maximum value of λ at which an unloading process was initiated. Note that λ_{ul} is associated with the onset of an unloading event and is not necessarily the hitherto maximum value of λ. Obviously, λ_{ul} represents the (reduced) current stiffness of the cohesive surfaces after damage and unloading have occurred. Also, one always has $\eta < 1$. While η_0 is the characteristic value of effective separation λ at which the effective traction σ (see below) for a cohesive surface pair reaches the strength T_{max} of the undamaged surface, λ_{ul} is the critical level of λ at which σ reaches the reduced strength $T_{max}(1-\eta)/(1-\eta_0)$ of the hitherto damaged cohesive surface pair.

The specific form for the potential is taken as

$$\Phi = \Phi(\lambda, \eta) = \begin{cases} \Phi_0\left(\dfrac{1-\eta}{1-\eta_0}\right)\left(\dfrac{\lambda^2}{\eta}\right), & \text{if } 0 \leq \lambda \leq \eta \\[2ex] \Phi_0\left(\dfrac{1-\eta}{1-\eta_0}\right)\left(1 - \dfrac{(1-\lambda)^2}{1-\eta}\right), & \text{if } \eta < \lambda \leq 1 \end{cases} \tag{3}$$

This relation allows the traction to be defined through

$$\mathbf{T} = \frac{\partial \Phi}{\partial \boldsymbol{\Delta}} \tag{4}$$

yielding the normal and shear traction components as

$$T_n = \sigma(\lambda, \eta)\frac{\Delta_n}{\lambda \Delta_{nc}} \quad \text{and}$$

$$T_t = \sigma(\lambda, \eta)\frac{\alpha \Delta_t}{\lambda \Delta_{tc}} \tag{5}$$

In the above expressions, $\alpha = \Delta_{nc}/\Delta_{tc}$ and

$$\sigma = \sqrt{(T_n)^2 + (T_t/\alpha)^2} = \begin{cases} \left(T_{max}\dfrac{1-\eta}{1-\eta_0}\right)\dfrac{\lambda}{\eta}, & \text{if } 0 \leq \lambda \leq \eta \\[2ex] \left(T_{max}\dfrac{1-\eta}{1-\eta_0}\right)\dfrac{1-\lambda}{1-\eta}, & \text{if } \eta < \lambda \leq 1 \\[2ex] 0, & \text{if } \lambda > 1 \end{cases} \tag{6}$$

For a surface that has previously been deformed to $\lambda = \eta$ and has experienced unloading from this value of λ, the work of separation for an arbitrary separation process is (see Eqs. (3) and (4))

$$\int_0^{\boldsymbol{\Delta}_c} \mathbf{T} \cdot d\boldsymbol{\Delta} = \Phi(1, \eta) \tag{7}$$

where $\boldsymbol{\Delta}_c$ is the critical separation under general mixed mode conditions at which σ vanishes and by definition $\lambda(\boldsymbol{\Delta}_c) = 1$. In particular, for pure normal separations $\boldsymbol{\Delta}_c = \{\Delta_{nc}, 0\}$ and for pure tangential separations $\boldsymbol{\Delta}_c = \{0, \Delta_{tc}\}$. Since the unloading and reloading along AP (Fig. 1(a)) are fully elastic, the amount of work required to fully separate a unit surface area from the undamaged state is

$$\int_0^{\boldsymbol{\Delta}_c} \mathbf{T} \cdot d\boldsymbol{\Delta} = \Phi(1, \eta_0) = \Phi_0 \tag{8}$$

This constant can be calibrated through pure normal and pure shear separations, i.e.,

$$\Phi_0 = \int_0^{\Delta_{nc}} T_n d\Delta_n = \int_0^{\eta_0 \Delta_{nc}} \left(T_{max}\frac{\Delta_n}{\eta_0 \Delta_{nc}}\right) d\Delta_n$$

$$+ \int_{\eta_0 \Delta_{nc}}^{\Delta_{nc}} \left(T_{max}\frac{1 - \dfrac{\Delta_n}{\Delta_{nc}}}{1-\eta_0}\right) d\Delta_n = \int_0^{\Delta_{tc}} T_t d\Delta_t$$

$$= \int_0^{\eta_0 \Delta_{tc}} \left(T_{max}\frac{\alpha \Delta_t}{\eta_0 \Delta_{tc}}\right) d\Delta_t + \int_{\eta_0 \Delta_{tc}}^{\Delta_{tc}} \left(\alpha T_{max}\frac{1 - \dfrac{\Delta_t}{\Delta_{tc}}}{1-\eta_0}\right) d\Delta_t$$

$$= \frac{1}{2}T_n^{max}\Delta_{nc} = \frac{1}{2}\alpha T_n^{max}\Delta_{tc}. \tag{9}$$

Apparently, $T_{max} = T_n^{max}$ is the maximum cohesive traction under conditions of pure normal separation.

While the bilinear relationship between σ and λ embodied in the above formulation is illustrated in Fig. 1(a), the variation of Φ is shown in Fig. 1(b). Overall, five parameters are needed to specify the cohesive behavior, including the maximum tensile strength T_{max}, the critical separations Δ_{nc} and Δ_{tc}, characteristic separation η_0, and α. Equation (6) describes a two-stage behavior as illustrated in Fig. 1. Between A and B ($0 \leq \lambda \leq \eta_0$), separation occurs elastically and the cohesive energy stored (work done in causing separation) is fully recoverable. Damage in the form of microcracks and other small-scale defects does not occur. Between B and C ($\eta_0 \leq \lambda \leq 1$), material degradation causes progressive reduction in the strength of the cohesive surfaces. This represents a phenomenological account of the effects of microcracks and other defects not explicitly modeled in the CFEM framework. Unloading from any point P follows path PA and subsequent reloading follows AP and then PC. Part of the work expended on causing the separation in this regime is irrecoverable, as indicated by the hysteresis loop ABP which implies dissipation during the softening process. Correspondingly, there is a decrease in the maximum tensile strength of the cohesive surface. This is reflected in the elastic reloading of the interface along AP and further softening along path PC. To correctly account for this behavior, it is necessary to record the value of λ_{ul}. We must point out that the dependence of the damaged behavior on previous deformation is very week and limited, only through η which tracks the hitherto largest extend of separation from which unloading has occurred. Any other aspect of preceding loading-unloading cycles does not in any way influence the deformation. This behavior is similar to the Markov chain (c.f., e.g., Lin [50]) in stochastic analyses.

Since any unloading and reloading (along PA in Fig. 1(a) or PA′ in Fig. 1(b)) are elastic, the amount of work that has been dissipated is

$$\Phi_d(\lambda, \eta)$$

$$= \begin{cases} 0, & \text{if } \lambda \leq \eta_0 \\[2ex] \Phi(\eta, \eta_0) - \Phi(\eta, \eta) = \dfrac{\eta - \eta_0}{1-\eta_0}\Phi_0, & \text{if } \eta_0 < \lambda \leq \eta \\[2ex] \Phi(\lambda, \eta_0) - \Phi(\lambda, \eta) = \dfrac{\lambda - \eta_0}{1-\eta_0}\Phi_0, & \text{if } \eta < \lambda \leq 1 \\[2ex] \Phi_0, & \text{if } \lambda > 1 \end{cases} \tag{10}$$

Note here that $\eta_0 < \eta = \max\{\eta_0, \lambda_{ul}\} < 1$ and that η never attains the value of 1. The dissipation is uniquely defined and $\Phi_d(\lambda, \eta)$ is a monotonically increasing function. When full separation is achieved, $\Phi_d(1, \eta) = \Phi_0$. Φ_d is partly converted into the surface energy and partly spent on causing damage in the material adjacent to crack surfaces through microcrack formation not explicitly modeled. A unique damage parameter can be defined to phenomenologically track the progressive softening of cohesive surfaces interspersed throughout the composite microstructure. This parameter D is defined such that

$$D = \frac{\Phi_d}{\Phi_0}. \tag{11}$$

Note that $0 \leq D \leq 1$, with $D = 0$ indicating fully recoverable interfacial separation and $D = 1$ signifying complete separation or total fracture. In the numerical analysis carried out in this paper and in Tomar et al. [1], D is used as a state variable quantifying the degree of the damage, providing a phenomenological measure for failure analysis. The spatial and time variation of $D = D(\mathbf{x}, t)$ allows the distribution and evolution of damage in various microstructures to be analyzed. Finally, it is important to remember that the development in this section is different from the interfacial cohesive laws for fatigue by Nguyen et al. [51], as reloading here follows the same path (AP in Fig. 1(a)) as unloading.

3 Finite Element Discretization

The finite element discretization leads to a system of linear algebraic equations of the form

$$\mathbf{M}\frac{\partial^2 \mathbf{U}}{\partial t^2} = -\mathbf{R}, \qquad (12)$$

where, $\mathbf{U}$ is the vector of nodal displacements, $\mathbf{M}$ is the nodal mass matrix, and $\mathbf{R}$ is the nodal force vector consisting of contributions from both the bulk elements and the cohesive surfaces, i.e., $\mathbf{R} = \mathbf{R}^b + \mathbf{R}^c$, where $\mathbf{R}^b = \int_V \mathbf{B}^T \mathbf{s} dV$ and $\mathbf{R}^c = \int_{S_{int}} \mathbf{N}^T \mathbf{T} dS$ denote the force vector contributions from bulk elements and cohesive surfaces, respectively. Here, $\mathbf{N}$ denotes the finite element shape function and $\mathbf{B}$ is the spatial gradient of $\mathbf{N}$. Krieg and Key [52] showed that from the point of view of accuracy as well as computational efficiency lumped mass matrix is preferable for explicit time integration procedures. Therefore, a lumped mass matrix $\mathbf{M}$ is used in Eq. (12) instead of the consistent mass matrix. The explicit time-integration scheme based on the Newmark β-method with $\beta = 0$ and $\gamma = 0.5$ is employed to integrate Eq. (12), cf. Belytschko et al. [53]. The displacements and velocities at $t_{n+1} = t_n + \Delta t_n$ are obtained by integrating the equations of motion using Newmark β-method as

$$\left.\begin{aligned} \frac{\partial^2 \mathbf{U}^{n+1}}{\partial t^2} &= \mathbf{M}^{-1}\mathbf{R}, \\ \frac{\partial \mathbf{U}^{n+1}}{\partial t} &= \frac{\partial \mathbf{U}^n}{\partial t} + \frac{1}{2}\Delta t_n\left(\frac{\partial^2 \mathbf{U}^{n+1}}{\partial t^2} + \frac{\partial^2 \mathbf{U}^n}{\partial t^2}\right), \quad \text{and} \\ \mathbf{U}^{n+1} &= \mathbf{U}^n + \Delta t_n\frac{\partial \mathbf{U}^n}{\partial t} + \frac{1}{2}(\Delta t_n)^2\frac{\partial^2 \mathbf{U}^n}{\partial t^2}; \end{aligned}\right\} \quad (13)$$

where $(\cdot)^{-1}$ denotes the matrix inverse. The time increment is taken to be Δt. The magnitude of Δt is based on the Courant-Freidrichs-Lewy criterion and material-related numerical stability considerations for explicit time integration.

4 Numerical Calculations

The issues analyzed in the numerical calculations are

a. The influence of microstructural morphology on dynamic fracture in the Al_2O_3/TiB_2 ceramic composite system.
b. The influence of phase size in the microstructures on fracture resistance of the materials.
c. The influence of interfacial bonding strength and loading rate on fracture behavior.
d. The correlation between fracture resistance and microstructural variation.

Two classes of microstructures are considered. The first class consists of idealized phase distributions with uniform TiB_2 particles embedded in an Al_2O_3 matrix. The microstructures considered in this case allow the effects of phase arrangement, phase shape and phase size to be systematically analyzed. The second class consists of digitized microstructures of actual Al_2O_3/TiB_2 ceramic composites. These microstructures have a range of phase morphology and sizes. Experiments have shown that these composites have different levels of fracture toughness and microstructure plays an important role in determining the behavior of these materials. In the analysis hereafter, both phases are assumed to be hyperelastic. However, the model and the approach are equally applicable to other constitutive behaviors.

4.1 Problem Analyzed. Computations are carried out for a center-cracked Al_2O_3/TiB_2 specimen under tensile loading. The specimen configuration is shown in Fig. 2. One half of the specimen is used in the calculations due to symmetry. The whole specimen has a height of $2W = 2.0$ mm and a width of $2H = 0.6$ mm for microstructures with idealized phase morphologies and of $2W$
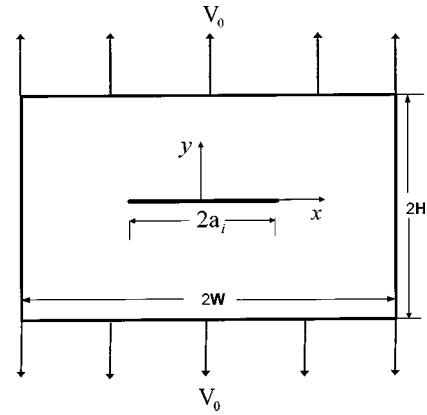

Fig. 2   Specimen configuration for calculations

$= 4.0$ mm and $2H = 0.6$ mm for actual microstructures. The length of the initial crack is $2a_i = 0.4$ mm for both types of specimen. The specimen is stress free and at rest initially. Tensile loading is applied by imposing symmetric velocity boundary conditions along the upper and the lower edges of the specimen. Conditions of plain strain are assumed to prevail. The finite element mesh used is shown in Fig. 3. The small region in front of the crack tip contains very fine mesh in order to resolve the intense stress field. This region contains one of the microstructures analyzed. The dimensions for this region are limited by the memory sizes of the Cray T90 and J90 computers used in this work. The particular dimension for this region is 40×500 μm in the case of the real micrographs and 80×300 μm for the hypothetical phase arrangements. These regions are much larger than the length scales involved in both types of microstructures. Thus, reasonable representations of the microstructures are achieved. The analyses carried out here are limited only to lengths of crack propagation within the microstructural regions. Material outside the microstructure window is assumed to be homogeneous and assigned effective properties representative of those for the Al_2O_3/TiB_2 ceramic composite (see Table 1). Both regions are discretized in the same manner, involving both bulk element and cohesive surface elements. For most of the results discussed here, the imposed boundary velocity is $V_0 = 2$ m/s for the top and bottom edges with a linear ramp from zero to this maximum velocity in the first 0.01 μs of loading. All other specimen surfaces have traction-free boundary conditions. This set of conditions represents the loading of the pre-crack by a tensile wave with a stress amplitude of 16.5 MPa ($\rho C_L V_0$) and a linear ramp from zero to that value in 0.01 μs. The properties of each segment of a potential fracture surface are specified according to its location inside the matrix or in the reinforcements or along the matrix/reinforcement interfaces. The constituent property values listed in Table 1 are used in the analysis.

Xu and Needleman [8] suggested that the maximum strength T_{max} should be between $E/1000$ and $E/200$ with E being the
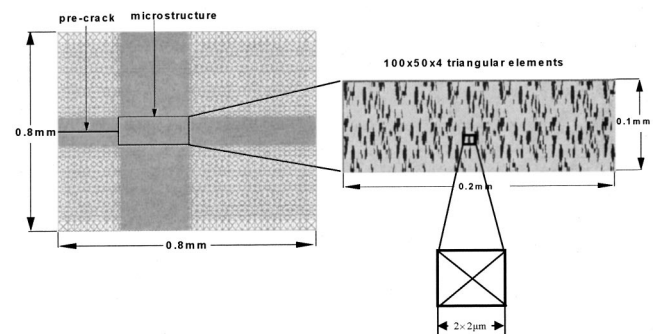

Fig. 3   Finite element discretization

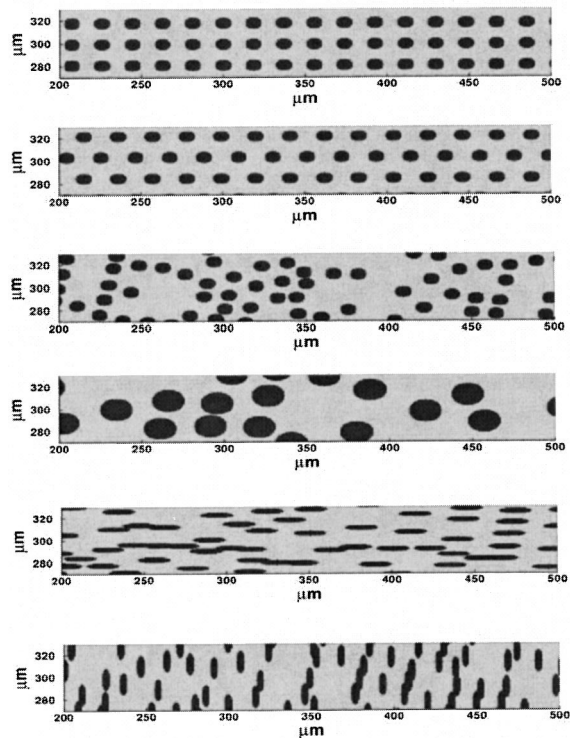**Fig. 4 Idealized microstructures**

Young's modulus. In this study, $T_{max}=E/700$ and $\alpha=1$ for each constituent and $\Phi_0=[(1-\nu^2)/E]K_{IC}^2$ with K_{IC} being the mode-I fracture toughness of the material in question. The critical separations Δ_{nc} and Δ_{tc} are calculated from Eqs. (8) and (9). The finite element mesh used consists of "cross-triangle" elements arranged in a quadrilateral pattern. Additionally, $\eta_0=0.001$ and the size of quadrilaterals in the mesh is taken as 2 μm, allowing the solution convergence criterion in Tomar et al. [1] for this type of CFEM models to be satisfied. Since interfaces in materials can have a range of bonding strength values arising from different processing methods, three variations of interfacial bonding strength are assumed for the real microstructures considered. These three levels are $T_{max}^{interface}=0.8T_{max}^{Al_2O_3}$, $T_{max}^{interface}=T_{max}^{Al_2O_3}$ and $T_{max}^{interface}=1.2T_{max}^{Al_2O_3}$. However, for most calculations carried out $T_{max}^{interface}=T_{max}^{Al_2O_3}$.

4.2 Idealized Microstructures. For the random microstructures of actual materials, morphological parameters are coupled and their effects can not be easily analyzed independently. To delineate the influence of phase attributes such as phase size, phase arrangement, phase shapes and phase size distribution, a series of idealized microstructures are generated and used in the numerical simulations. These microstructures are shown in Fig. 4. The volume fraction of the TiB$_2$ phase in these microstructures is

30%. Variations in the arrangement, size, and shape of the TiB$_2$ particles are considered. Specifically, four types of particle arrangements (a total of six microstructures) are considered. They are

  a. uniformly distributed circular particles in a square array (Fig. 4(a))
  b. uniformly distributed circular particles in staggered array (Fig. 4(b))
  c. randomly distributed circular particles (Figs. 4(c,d))
  d. randomly distributed unidirectional elliptical particles (Figs. 4(e,f))

These microstructures allow the effects of particle arrangement (A, B, and C), particle size (C and D), particle shape (C and E), and particle orientation (E and F) to be characterized.

Microstructure A (Fig. 4(a)) consists of a regular array of uniform particles with a square unit cell. The two axes of symmetry (x and y) cause the overall response to be orthotropic. The staggered particle arrangement in microstructure B (Fig. 4(b)) has a hexagonal unit cell causing it to be isotropic. Microstructures C and D (Figs. 4(c) and 4(d)) have randomly distributed circular particles that differ in size. For microstructures A, B, and C, the particles have a radius of 5 μm, while the particle radius is 10 μm for microstructure D. Nonetheless, the volume fraction of the TiB$_2$ phase is fixed at 30% for all the microstructures.

The randomly distributed unidirectional elliptical particles (E and F) give rise to orientation-dependent fracture response. To simplify the analysis, two extreme cases with elliptical reinforcements are considered. The long and short axes of the TiB$_2$ particles are 10 μm and 2.5 μm, respectively, giving rise to an aspect ratio of 4. Microstructure E (Fig. 4(e)) is representative of microstructures in which elliptical particles with the major axis aligned in the direction of the apparent crack path are randomly distributed. The area/volume fraction of the particles is the same as that of microstructures A, B, and C. Microstructure F (Fig. 4(f)) has a similar phase morphology as microstructure E, except that the minor axis of the elliptical particles is aligned in the direction of the apparent crack path. Microstructures E and F allow the effect of phase orientation on fracture to be analyzed. The characteristics of all microstructures are summarized in Table 2. Numerical simulations using the six microstructures allow the delineation of the effect of range of variation in the morphology of microstructures on the dynamic fracture behavior of Al$_2$O$_3$/TiB$_2$ ceramic composites. In order to account for statistical variations with arrangement of second phase in microstructures, four different random samples (only one is shown here) of each of microstructures C, and D are used simultaneously to carry out multiple calculations. To illustrate the levels of variation in the results, the time histories of the apparent crack length (projection of crack length in the x-direction) for microstructure D is shown in Fig. 5. Significant variations are seen. The variations of the apparent crack length for microstructure D are approximately 30% around the mean value. This indicates that the size, shape and distribution of the particles greatly affect the degree of variations in behavior, not just the average behavior. In light of this, it is obvious that statistical characterizations of response require a sufficiently large number of

Table 2 Characterization of idealized Al$_2$O$_3$/TiB$_2$ microstructures

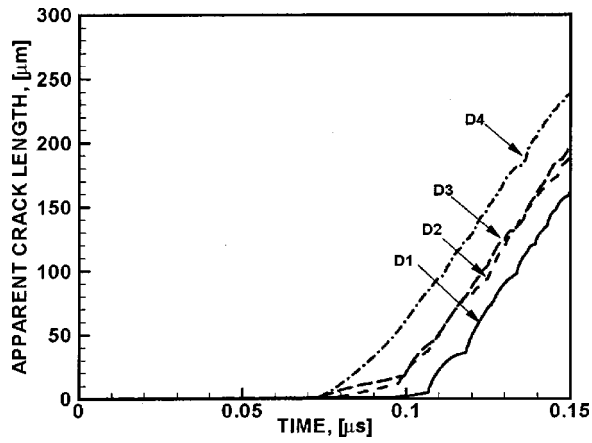| Microstructure	Arrangement of Particles	Dimension of Particles (μm)	Shape of Particles	Mean Linear Intercept Length in TiB$_2$	Average Energy Release Rate $\partial\Phi/\partial a$ (J/m)
A	Rectangular	a=b=5	Circular	7.85	46.2
B	Hexagonal	a=b=5	Circular	7.85	39.3
C	Random	a=b=5	Circular	7.85	36.2
D	Random	a=b=10	Circular	15.7	34.9
E	Random	a=10, b=25	Elliptical	15.7	35.1
F	Random	a=25, b=10	Elliptical	3.98	50

Fig. 5 Time histories of crack length in microstructure D

Fig. 7 Stress contours of maximum principle stress σ_{max} (MPa) in microstructures A–F at t=0.15 μs

samples. Such statistical analyses have to be carried out for different arrangements of phases rather than for random interfacial and constitutive properties which give rise to variations for different reasons. The need for multiple samples for statistical analyses is also partly attributed to the fact that the two phases in the hypothetical microstructures are not fully intermixed. Therefore, possibilities for variations in responses are larger. Relatively small numbers of microstructural samples may be sufficient for a characterization in variations if the two phases are more intimately mixed in a random manner. This is often the case with real microstructures. It is partly because of this reason that we have not pursued a full statistical variation analysis for the hypothetical microstructures here. Rather, we will discuss in Sec. 2.3 characterization of this effect for microstructures of actual materials which show more randomly distributed, intimately mixed phases. A combined deterministic and stochastic analysis is carried out in Tomar and Zhou [54–55]. Here, we focus our discussion on the first sample of microstructure C (i.e., Cl) and the first sample of microstructure D (i.e., D1).

The crack and damage patterns at t=0.15 μs for microstructures A, B, C1, D1, E, and F are compared in Fig. 6. The phase boundaries are outlined by solid dark lines for clear visualization of the phase morphologies. Contours of the maximum principle stress σ_{max} for these microstructures are plotted in Fig. 7. The time histories of the total crack length $\ell(t)$ (sum of crack surfaces generated in (two-dimensions) in the microstructures are shown in Fig. 8. Note that $\ell(0)$=0, therefore, crack lengths referred to here concern new crack surfaces/length generated and do not include length of the initial crack. The time histories of the apparent crack length for all the cases considered so far are shown in Fig. 9. The
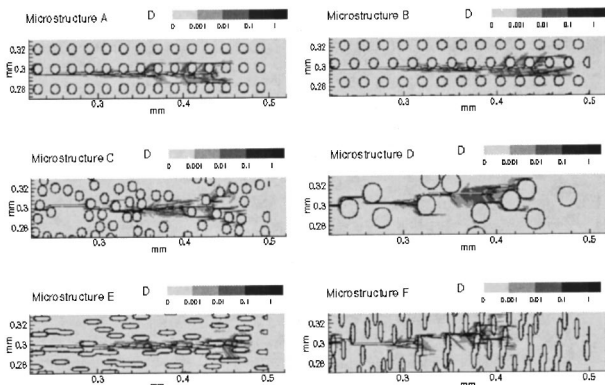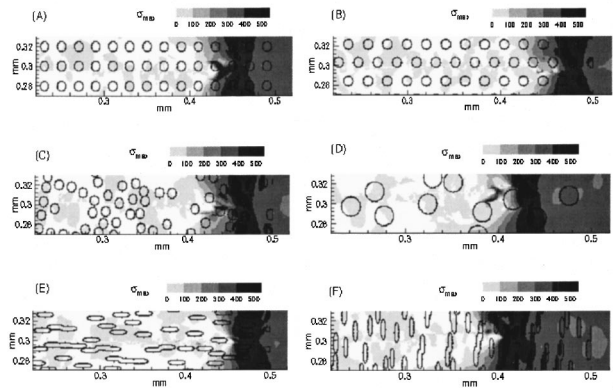
time histories of overall energy dissipated ϕ_d are plotted in Fig. 10. The energy dissipated is due to the crack surface separation and microcrack nucleation. It is one measurement of the fracture resistance of materials under the conditions analyzed. The overall energy dissipated ϕ_d is the sum of cumulative energy dissipated in all the damaged cohesive surfaces, i.e., $\phi_d = \int_{S_d} \Phi_d dS$, where S_d represents surface area of cohesive surfaces with damage. By plotting ϕ_d as a function of the apparent crack length a (see Fig. 11), we can readily obtain the average energy release rate ($\bar{G} = \phi_d/a$) which provides a quantitative measure for the dynamic fracture resistance of the materials (Fig. 12). To facilitate analysis,
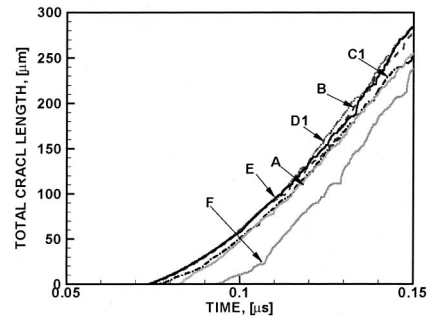

Fig. 8 Time histories of total crack length in idealized microstructures
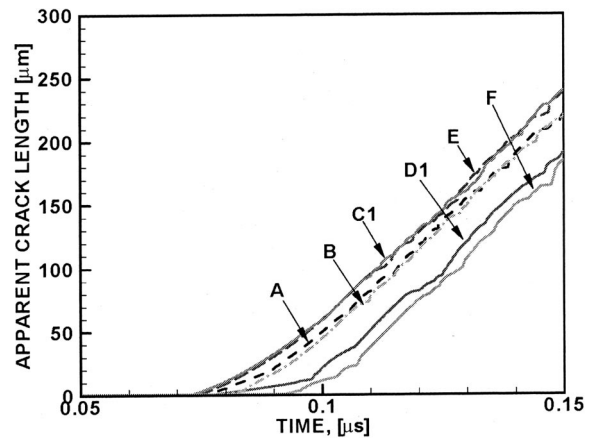

Fig. 6 Damage evolution in microstructures A–F at t=0.15 μs

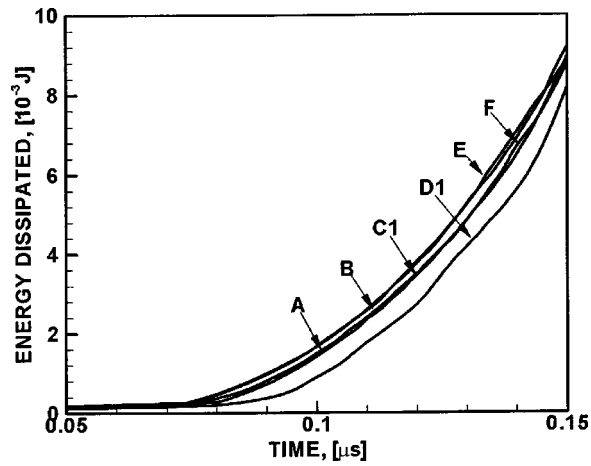**Fig. 9 Time histories of apparent crack length in idealized microstructures**

Fig. 10 Time histories of energy dissipated in idealized microstructures
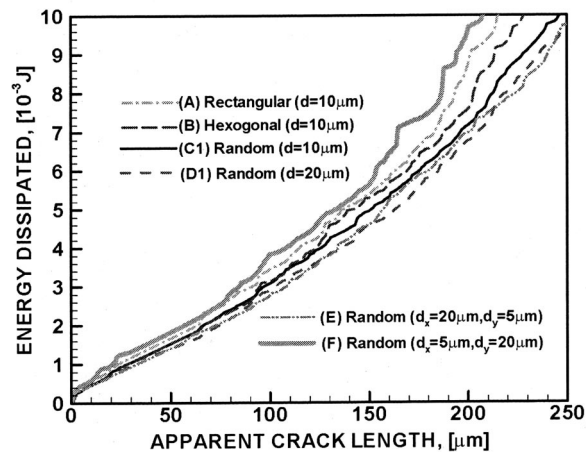

Fig. 11 Energy dissipated as a function of apparent crack length for idealized microstructures
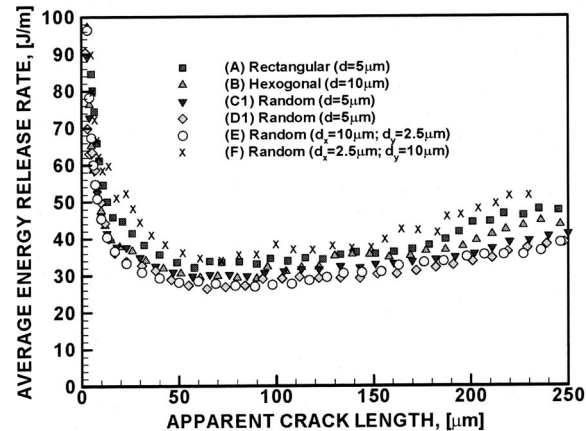

Fig. 12 Comparison of average energy release rate in the idealized microstructures

the average energy release rate for each microstructure is listed in Table 2. This value is calculated for the first 200 μm of the apparent crack length. It is noted that it takes different amounts of time for the apparent crack length to reach 200 μm in different microstructures.

4.2.1 Crack Growth and Damage Evolution in the Microstructures. Figure 6 shows that the distribution of damage is influenced by the material heterogeneity in the microstructures. Damage is more likely to occur along the interfaces and inside the matrix. Clearly, the TiB_2 particles represent stronger obstacles to crack propagation due to their higher bulk modulus and cohesive strength. It can be seen that when the crack approaches a particle it would alter its direction of propagation to circumvent the obstacle by progressing mainly along the interface. When the TiB_2 particles are not in the immediate path, the crack would propagate horizontally along the direction of the apparent crack path. Away from the main crack, microcracks form along the particle/matrix interface and inside the Al_2O_3 matrix. The formation of microcracks provides opportunities for the main crack to branch. However, most of the microcracks arrest shortly after nucleation and do not propagate over a long distance. The crack follows a microscopically zigzag path between particle clusters. Nevertheless, overall crack propagation is in the horizontal direction. It is clear that fracture occurs primarily along phase boundaries and inside the matrix. Continuous and favorably oriented interfaces (parallel to the direction of crack propagation) facilitate crack growth.

The contours of the damage parameter D indicate that dissipation through microcracking occurs away from the main cracks. The patterns also reveal the attempts of the crack to branch out in different directions.

4.2.2 Effects of Phase Arrangement. Figure 6 shows that crack growth and development in different microstructures exhibit similar characteristics while the details of crack path and fracture outcome are highly dependent on the particular microstructural phase distribution. This observation is clearly seen in Fig. 5 as well, where the crack length histories are significantly different among the four samples of microstructure D (larger particle size compared with microstructure C). Note that the difference is much smaller among the results for the four samples of microstructure C. Clearly, the larger particle size in samples of microstructure D provides higher perturbations to crack propagation compared with microstructure C. This causes the fracture process to be sensitive to phase arrangement over the length scale studied.

Microstructures A, B and C have the same TiB_2 particle diameter of 10 μm. In microstructures A and B, the crack tends to circumvent the hard particles and grow along a straight path in the matrix or along interfaces in early stages of propagation, see Fig. 6. The crack shows attempts to branch out after propagating for a short distance, as indicated by the contours of the failure parameter D. In microstructure C, the crack path exhibits significant fluctuations due to the random distribution of the particles. In all three microstructures, damage and crack branching attempts intensify in later stages of crack development. This is mainly due to the increasing crack velocity, cf. Johnson [56]. Despite the differences, the histories of the apparent crack length in microstructures A and B are similar (Fig. 9).

Despite the differences in the microstructures, the characteristics of the stress fields over the long-range are similar (Fig. 7). However, the details over the short range in the vicinity of the crack tip are significantly different. Obviously, the differences occur over a similar length scale as that for the microstructural heterogeneities.

The time histories of energy dissipated for the idealized microstructures are shown in Fig. 10. The dissipation rate is lower initially and accelerates throughout the deformation. The energy dissipated is shown as a function of the apparent crack length in Fig. 11. Although the time history profiles in Fig. 10 are similar, Fig. 11 shows that the microstructures with regular particle arrange-
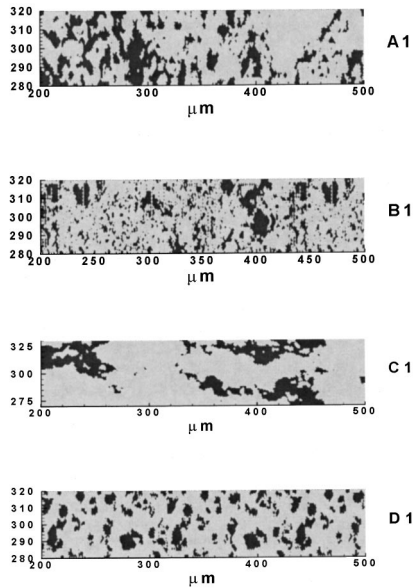
Fig. 13 Real microstructures A1–D1

Fig. 14 Damage evolution in microstructure D1

ments (A and B) exhibit somewhat higher levels of energy dissipation than the microstructures with random particle arrangements (C and D). This indicates that regular particle arrangements represent more significant obstacles to crack propagation in terms of energy dissipation per unit crack advancement in the *x*-direction. In particular, microstructure A shows the highest level of energy dissipation among A, B, and C.

4.2.3 Effects of Phase Size. The results in Fig. 5 show that crack path exhibits significant variations in microstructures with the larger particle size. The variations at least partly come from the larger inter-particle spacing in microstructure D. The larger particle size also causes the crack speed to vary significantly among samples of microstructure D. On the basis of energy dissipation per unit apparent crack length, Fig. 11 and Table 2 show that the energy dissipation rate in microstructure C is higher than that in microstructure D at the same value of apparent crack length. This indicates that microstructure C with random distribution of smaller particles has a higher fracture resistance than microstructure D. The approximately 5–10% higher average energy release rate for microstructure C in Table 2 is primarily due to the more frequent perturbations from the smaller particles in microstructure C.

4.2.4 Effects of Microstructural Anisotropy. Figures 6 and 7 also show that the crack growth in microstructures E and F displays distinctive patterns, primarily because of their different particle orientations. In microstructure E, the crack propagates along a fairly straight path inside the matrix or along the interface between the phases with less chance of encountering hard particles. In microstructure F, the crack path is more oscillatory due to an increased likelihood of encountering second phase obstacle par-
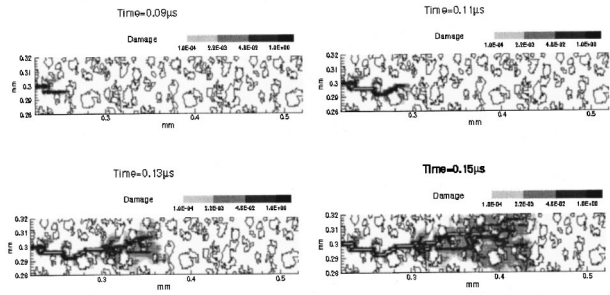
ticles. Crack initiation occurs at approximately 0.07–0.08 μs in microstructures A to E. However, crack initiation is at 0.095 μs in microstructure F, indicating significant retardation by the orientation of the particles. The higher resistance to crack growth of microstructure F is also reflected in the smaller crack length and lower crack speed seen for it in Fig. 9. In Fig. 12, the energy dissipated per unit apparent crack length (called the "energy release rate" hereafter) is shown for all the microstructures analyzed so far. Both Figs. 11 and 12 show that microstructure F demonstrates clearly higher energy release rate than the other microstructures. This is mainly due to the bridging effect of elongated particles perpendicular to the direction of crack propagation. In contrast, microstructure E has an energy release rate similar to that of microstructure C.

4.3 Real Microstructures. Figure 13 shows one sample for each of the four types of real microstructures used in simulations here. Four samples for each type are used (but not shown here) for a quantification of the variations in results. Microstructures A and C contain connected TiB_2 in an Al_2O_3 matrix. On the other hand, microstructures B and D consist of TiB_2 particles surrounded by the Al_2O_3 phase. There is a significant difference in the size scales of the phases among the four microstructures. The average linear intercept length for each of the phases is shown in Table 3 to provide a parametric quantification of the size scales of these microstructures.

4.3.1 Crack Growth and Damage Evolution. In order to account for the damage and fracture evolution in the four microstructures, distributions of the damage parameter D and the maximum principle stress σ_{max} are obtained at different times. The results for microstructure sample D1 are discussed. As shown in Fig. 14, contours of the damage parameter D at four times are used to facilitate visualization of damage evolution and crack development. In addition, contours of σ_{max} are plotted in Fig. 15 to show the evolution of near-tip stress field. The crack grows along a straight path into the matrix between small TiB_2 particles and then arrests when the crack tip impinges on a particle, Figs. 14(a,b). This particle represents a stronger obstacle to crack growth due to its higher bulk and cohesive strengths. Afterwards, the crack circumvents the impeding particle through the separation of particle/matrix interface. Part of the debonding process involves primarily local tangential (shear) displacement along the

Table 3 Characterization of digitized Al_2O_3/TiB_2 microstructures

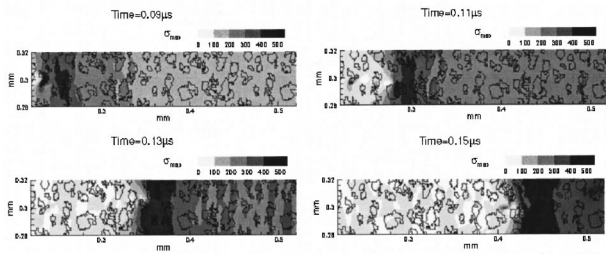| Microstructure	Average Intercept Length of TiB_2 (mm)	Average Intercept Length of Al_2O_3 (mm)	$\partial\Phi/\partial a$ (J/m) (Strong Interface)	$\partial\Phi/\partial a$ (J/m) (Intermediate Interface)	$\partial\Phi/\partial a$ (J/m) (Weak interface)
A	5.06	10.3	58.7	52	55
B	2.43	5.88	59.2	55.5	54.5
C	11.31	24.77	51	49	46
D	3.09	8.17	58.2	50	54.6

Fig. 15 Contours of maximum principle stress σ_{max} (MPa) in microstructure D1

interface. Subsequent propagation is primarily through the matrix and interfaces between small particles and the matrix. Along with the main crack propagation, micro-separation occurs in the form of attempted crack branching as shown at 0.13 μs in Fig. 14(c). However, the micro-separation fails to develop into a macro crack branch and one main crack front exists, Figs. 14(d) and 15(d).

The results in Figs. 14 and 15 show that the crack path is significantly influenced by the microstructural phase morphologies. Since fracture occurs primarily along phase boundaries and inside the matrix, crack path is highly dependent on the specific phase morphology. For instance, for microstructures B and D, the crack paths demonstrate more oscillations than those for microstructures A and C. This is because cracks are forced to propagate along the phase boundaries between relatively larger Al_2O_3 islands and TiB_2 networks.

4.3.2 Crack Length History. The time histories of apparent crack length for the four microstructures are shown in Fig. 16. The four different curves in each plot represent the results for the four random samples of each microstructure. It can be seen that the microstructural variations do not significantly influence the fracture initiation time under the conditions studied. The crack initiates at approximately 0.075 μs in all the microstructures. Short periods of plateau are observed in Figs. 16(a,c), indicating temporary arrests of the crack propagation due to impediments by hard particles. Obviously, the apparent crack velocities (the time rate of change of apparent crack length) in microstructures B and D are statistically higher than those for microstructures A and C, imply-
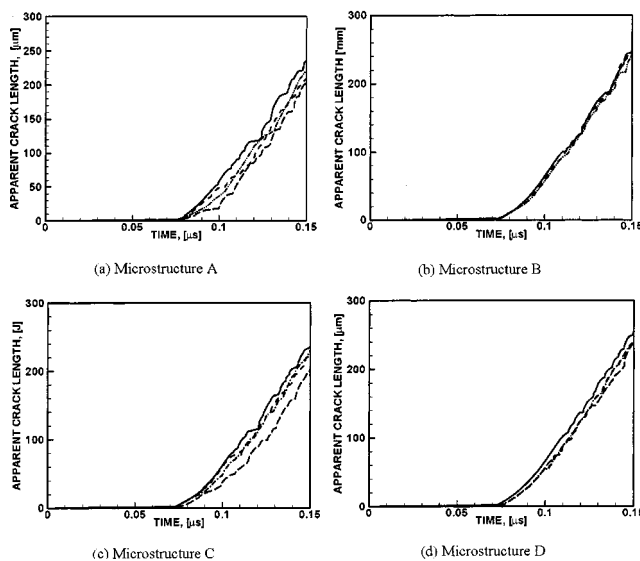
ing faster crack propagation in microstructures that contain relatively fine TiB_2 phase dispersed in continuous Al_2O_3 matrix.

4.3.3 Energy Release Rate. Figure 17 shows the time histories of energy dissipated Φ_d in the four microstructures. In order to compare the fracture resistance among the microstructures Φ_d is also shown as functions of the apparent crack length in Fig. 18. The curves represent the average values of Φ_d for each microstructure. The error bars along the curves indicate the range of values among the four random samples for each microstructure. Under the conditions given, the difference in energy release rate is within 15% among these microstructures. To facilitate comparison, the average energy release rate $\bar{G}$ at an apparent crack length of $a = 250$ μm is also plotted in Fig. 19 and listed in Table 3 as a function of the linear intercept length for TiB_2. Three different levels of bonding strength (weak, intermediate and strong, see the

Fig. 17 Time histories of energy dissipated in the four real microstructures

Fig. 16 Time histories of apparent crack length in the four real microstructures

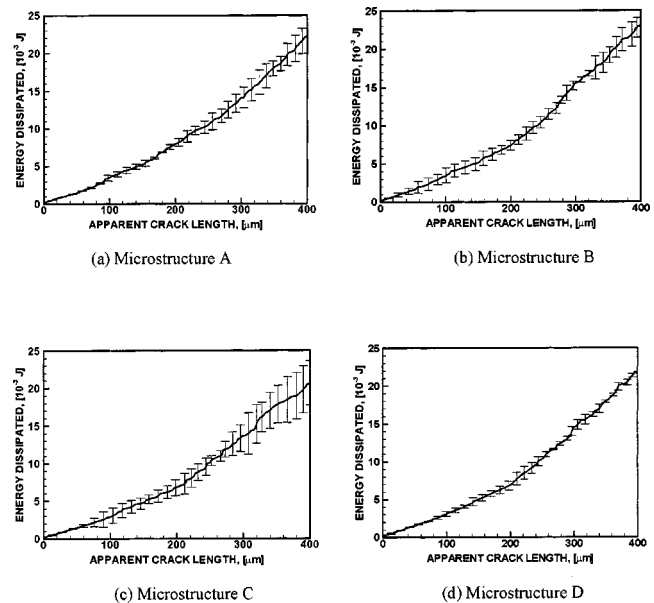**Fig. 18 Energy dissipated as a function of apparent crack length in the four real microstructures**
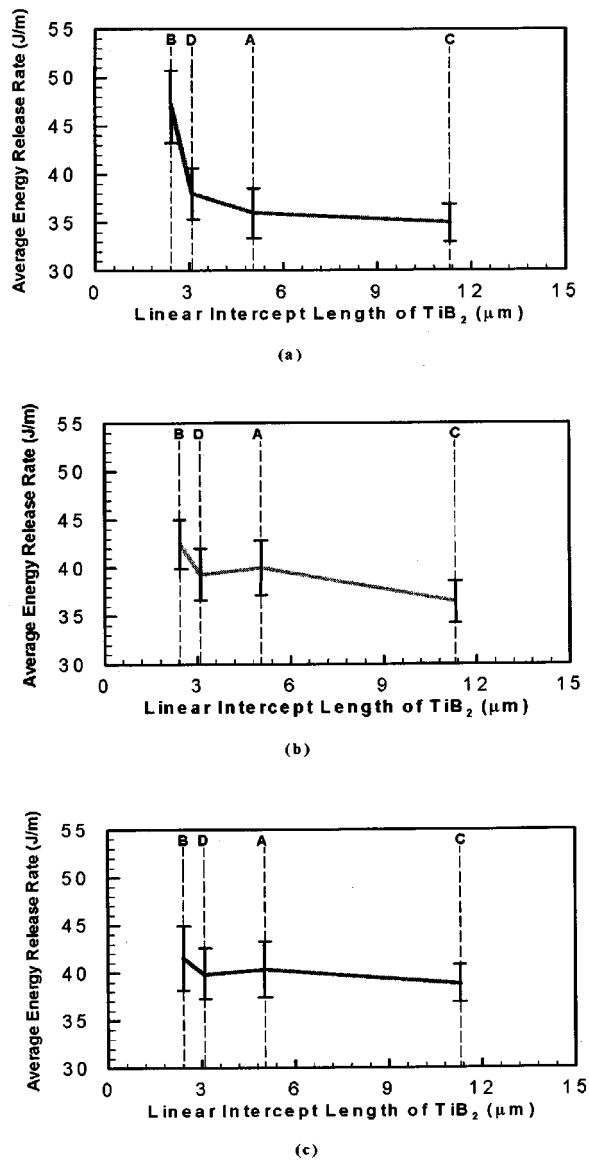
Fig. 19 Comparison of average energy release rate in the four real microstructures with different interfacial bonding strengths

next section for more discussion) between the two phases are considered. For the strong interface (Fig. 19(c)) microstructure B has an average energy release rate of approximately 42 J/m. This value is about 10% higher than that for microstructure C. Microstructure A has an average release rate of 40 J/m which is about 5% lower than that for microstructure B. Microstructure D has an average energy release rate about 4% higher than that for microstructure C. It can be seen that microstructures containing evenly distributed fine particles tend to have higher fracture resistance. The error bars in Fig. 19 show that variations in the range of energy release rate decreases with the average intercept length. Among the four microstructures, microstructure C has rather unique phase morphology. Experiments show that this microstructure exhibits the lowest fracture resistance (cf. Logan [47]). Indeed, the calculated results here show the same trend as that in the experiments. It appears that continuous and favorably oriented Al_2O_3/TiB_2 boundaries inherent in microstructure C allow cracks to propagate with relatively low hindrance and cause the fracture resistance to be lower in this microstructure compared with other microstructures.
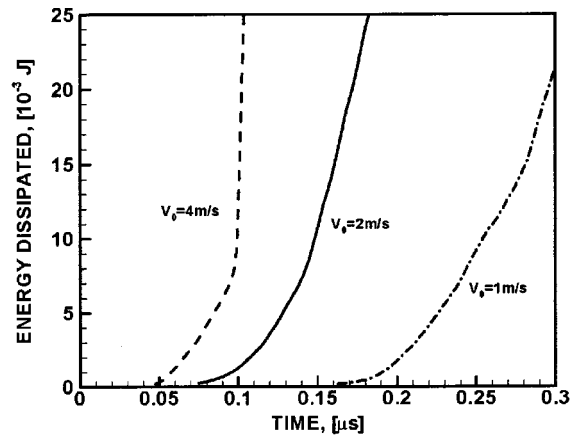
4.3.4 Effects of Different Interfacial Bonding Strengths. A range of interfacial bonding strength values along the interface between TiB_2 and Al_2O_3 can arise from different processing methods and conditions. It is very difficult to measure the interfacial bonding strength directly because of the small phase size and complicated phase morphologies. Therefore, a parametric study of the effects of interfacial bonding strength is carried out. Three levels of interfacial bonding strength values with $T_{max}^{interface} = 0.8 T_{max}^{Al_2O_3}$, $T_{max}^{interface} = T_{max}^{Al_2O_3}$ and $T_{max}^{interface} = 1.2 T_{max}^{Al_2O_3}$ are considered. These values represent weak, intermediate and strong interfaces, respectively. Average energy release rates for the four real microstructures with the weak ($T_{max}^{interface} = 0.8 T_{max}^{Al_2O_3}$), intermediate ($T_{max}^{interface} = T_{max}^{Al_2O_3}$) and strong ($T_{max}^{interface} = 1.2 T_{max}^{Al_2O_3}$) interfacial bonding strengths at an apparent crack length of $a = 250 \mu m$ are plotted as functions of linear intercept length of TiB_2 in Figs. 19(a), 19(b), and 19(c), respectively. The results demonstrate that, for all three levels of interfacial bonding strength, microstructure B has the highest average energy release rate and microstructure C has the lowest. The differences among the energy release rate levels for the four microstructures vary with interfacial bonding strength. For instance, in the case of strong interfacial bonding strength ($T_{max}^{interface} = 1.2 T_{max}^{Al_2O_3}$), the average energy release rate for microstructure B is approximately 10% higher than that for microstructure C. However, in the case of the weakest interfacial bonding strength ($T_{max}^{interface} = 0.8 T_{max}^{Al_2O_3}$), the average release rate for microstructure B is approximately 20% higher than that for microstructure C. These results also reflect an enhancing influence of microstructure on fracture resistance as the interfacial bonding strength decreases.

In order to decouple the effects of interfacial bonding strength and microstructure variation, an analysis is carried out on microstructure D at different levels of interfacial bonding strength. Five different levels of interfacial bonding strength are chosen. From the proportional relationship between the surface energy Φ and the maximum cohesive strength T_{max}, we know that the five levels of interfacial bonding strength correspond to five levels of surface energy of interface Φ_i, where Φ_i, Φ_A, and Φ_T denote the cohesive energy of interfaces, Al_2O_3 and TiB_2 phases, respectively. The first two levels represent strong bonding between the phases. These levels are chosen to be the same as that of TiB_2 or Al_2O_3, i.e., $T_{max}^{interface} = T_{max}^{TiB_2}$ ($\Phi_i = \Phi_T$) or $T_{max}^{interface} = T_{max}^{Al_2O_3}$ ($\Phi_i = \Phi_A$). The third level of $T_{max}^{interface}$ is chosen as half of that of Al_2O_3, i.e., $T_{max}^{interface} = 0.5 T_{max}^{Al_2O_3}$ ($\Phi_i = 1/2\Phi_A$). This level is intended to represent a somewhat weaker bonding between the phases. The fourth and fifth levels of $T_{max}^{interface}$ are designed to represent relatively weaker interfaces with $T_{max}^{interface} = 0.25 T_{max}^{Al_2O_3}$ ($\Phi_i = 1/4\Phi_A$) and $T_{max}^{interface} = 0.1 T_{max}^{Al_2O_3}$ ($\Phi_i = 1/10\Phi_A$), respectively.
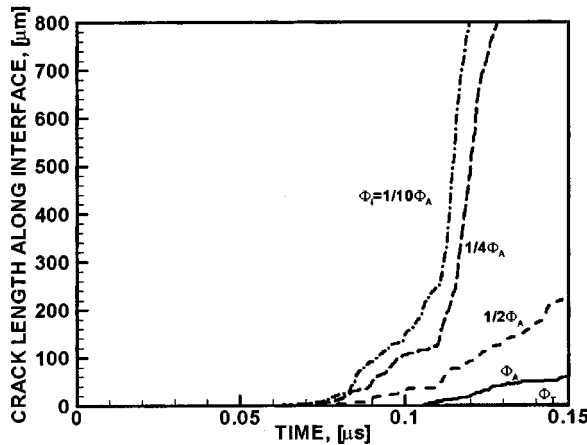
4.3.4.1 Time history of crack length. Figures 20(a) and (b) show the time histories of cumulative crack lengths in the Al_2O_3 phase and along the interfaces between Al_2O_3 and TiB_2, respectively. The results for the crack length in TiB_2 are not shown in the figure since fracture in this phase is negligible. The profiles show the crack initiation at $t = 0.072 \mu s$ for all the cases. The mode of failure dramatically influences the distribution of crack length in different phases. Clearly, the crack length along the interfaces gradually increases with decreasing interfacial bonding strength. Upon transition of the failure mode from main crack propagation as in the cases of $T_{max}^{interface} = T_{max}^{TiB_2}$, $T_{max}^{interface} = T_{max}^{Al_2O_3}$ and $T_{max}^{interface} = 0.5 T_{max}^{Al_2O_3}$ to microcrack nucleation as in the cases of $T_{max}^{interface} = 0.25 T_{max}^{Al_2O_3}$ and $T_{max}^{interface} = 0.1 T_{max}^{Al_2O_3}$, the crack length along the interfaces increases significantly. This dramatic increase is due to simultaneous formation of microcracks along multiple weak interfaces.
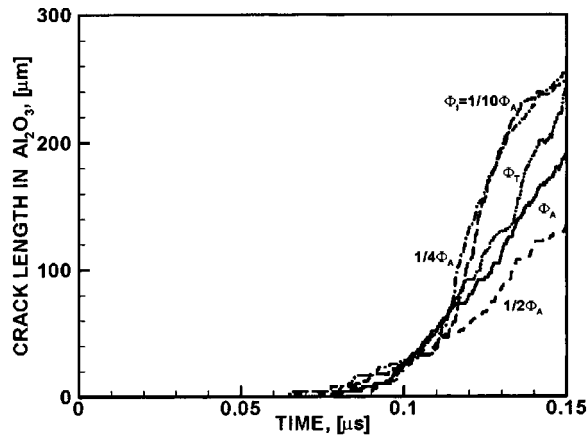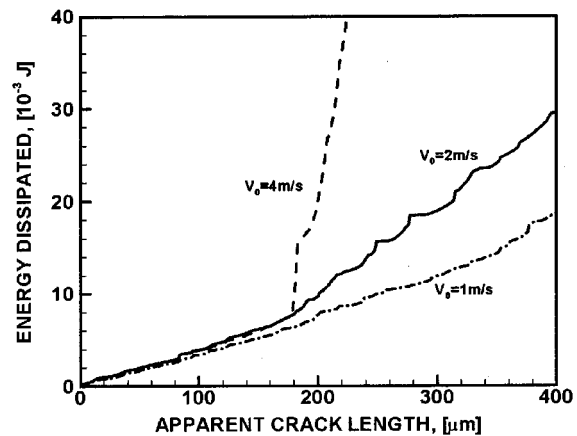
(a) in the Al$_2$O$_3$ phase

(b) along the Al$_2$O$_3$ / TiB$_2$ interface

Fig. 20 Comparison of crack length histories in microstructure D with different interfacial bonding strenghts

(a) Energy dissipated as a function of time

(b) Energy dissipated as a function of apparent crack length

Fig. 22 Comparison of energy dissipated and energy release rate for different loading rates

4.3.4.2 Time history of energy dissipated. Figure 21 shows the evolution of energy dissipated Φ_d for microstructure D. The initial macroscopic crack begins to grow at about 0.07 μs and extends along the interface in the microstructure. The nucleation and coalescence of microcracks takes place shortly after the crack

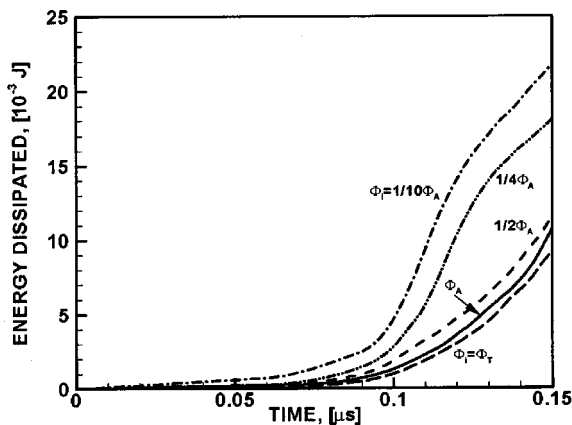**Fig. 21 Time histories of energy dissipated for microstructure D with different interfacial bonding strengths**

starts to grow. Clearly, the energy dissipated increases with decreasing interfacial bonding strength. Under the conditions analyzed, simultaneous formation of microcracks and their coalescence allow more energy to be dissipated in composites with weak interfacial bonding strengths than in composites with strong interfacial bonding strengths. Note that in the cases of $T_{max}^{interface} = 0.25T_{max}^{Al_2O_3}$, and $T_{max}^{interface} = 0.1T_{max}^{Al_2O_3}$, the rate of increase of energy dissipated Φ_d becomes lower at about $t = 0.12$ μs. This corresponds to a shift of cracking toward the interface and away from the matrix. Note that the work of separation for interfaces is much lower than that for Al$_2$O$_3$ and TiB$_2$.

4.3.5 Effect of Loading Rate. Loading rate has a clear impact on dynamic behavior of materials, primarily due to the inertial effect. Experiments conducted by Ravi-Chandar and Knauss [57–60] revealed many characteristics of dynamic fracture under different loading rates. In particular, they found that the dynamic fracture toughness increases when a crack accelerates. This trend becomes more significant at higher loading rates. An apparent loss of a unique relation between stress intensity factor and crack tip velocity at high crack velocities was also observed in their experiments. Johnson [56] employed a cell model to study dynamic crack propagation in homogeneous materials by taking into account the evolution of crack tip process regions. His results fur-

ther explain that dynamic fracture toughness is not a unique function of crack velocity at high crack velocities, but is also dependent on crack acceleration. It is of great interest to study the interaction between microstructure and loading rate effects. Multiple length scales in a microstructure give rise to more complicated interactions under dynamic loading. Crack tip instabilities including deflection and branching, can arise form the combined influence of microstructure and higher loading rates.

Different loading rates are achieved by varying the boundary velocity imposed on the upper and the lower surfaces of specimen. Three boundary velocities $V_1 = 1$ m/s, $V_2 = 2$ m/s and $V_3 = 4$ m/s result in input stress waves with magnitudes ranging from approximately 8 MPa to 32 MPa. Microstructure D is used. Figure 22 shows the energy dissipated as a function of the time and apparent crack length for different loading rates. Clearly, the average energy release rate increases with loading rate, indicating more extensive damage at higher stress levels arising from higher loading rates. This trend becomes more significant as the crack length increases. Since crack acceleration is found to increase with loading rate in the calculations here (not shown), this result echoes the findings of Ravi-Chandar and Knauss [57–60] and Johnson [56] in that the energy release rate is not just a function of crack velocity, it also depends on crack acceleration.

5 Concluding Remarks

The failure of Al_2O_3/TiB_2 ceramic composites due to fracture under dynamic loading is analyzed. The framework of analyses uses the CFEM with a bilinear cohesive law. Analyses are carried out using idealized phase morphologies as well as the micrographs of real microstructures produced by Logan [47]. These microstructures are used to investigate the effects of phase arrangement, phase size, and phase shape on damage and fracture evolution. The results demonstrate that microscopic phase distribution and phase size scale significantly influence the fracture behavior. For the idealized microstructures containing circular particles, the microstructures with orderly arranged particles demonstrate higher fracture resistance than the microstructures with randomly arranged particles. The particle size also has significant influence on the fracture resistance of the microstructures. It is found that microstructures with fine particles show higher fracture resistance than those with larger particles. The orientation-dependence of the fracture resistance is also investigated through the consideration of second phase elliptical inclusions. When the crack path is perpendicular to the major axis of elliptical particles, the fracture resistance of the microstructures is considerably higher as compared with the case with the crack path being parallel to the major axis.

A significant variation in the average energy release rate is observed among the four different microstructures of actual Al_2O_3/TiB_2 ceramic composites. Microstructures with evenly distributed finer particles are found to yield higher fracture resistance. Calculations show that failure mode is significantly influenced by the interfacial bonding strength between the phases. When weak interfacial bonding exists, microcrack initiation and growth is the principal mode of failure. Whereas when strong interfacial strength is derived from material processing, the advancement of a dominant crack and crack branching are observed. Under the conditions studied, the simultaneous formation of microcracks and their coalescence in a material with weak interfacial bonding allow more energy to be dissipated than in a material with strong interfacial bonding. The results also show that the damage evolution, crack growth and energy release rate are strongly dependent on loading rate. Due to the inertial effect, the energy release rate increases with loading rate. These findings are in good agreement with experimental results reported by Ravi-Chandar and Knauss [57–60] and Logan [47]. Additionally, the general trends in the behavior of the Al_2O_3/TiB_2 composites seen here are consistent with the experimental findings of Keller and Zhou [61].

Finally, we point out that this study does not account for the stochastic variations of bulk and interfacial properties in each of the constituents and along the interphase interfaces in the microstructures. Such an analyses has been carried out and reported by Tomar and Zhou [54–55]. The study there uses a second order perturbation analysis to systematically characterize the effects of material property variations on fracture process and fracture resistance. A deterministic analysis and a stochastic analysis are integrated and carried out simultaneously. The benefit is that both the explicit fracture outcome and the range of variation of the outcome in terms of crack length, crack speed, and fracture resistance are obtained.

References

[1] Tomar, V., Zhai, J., and Zhou, M., 2004, "Bounds for Element Size in a Variable Stiffness Cohesive Finite Element Model," to appear in Int. J. Numer. Methods Eng.

[2] Needleman, A., 1987, "A Continuum Model for Void Nucleation by Inclusion Debonding," ASME J. Appl. Mech., **38**, pp. 289–324.

[3] Tvergaard, V., 1990, "Effect of Fibre Debonding in a Whisker-Reinforced Material," Mater. Sci. Eng., A, **125**, pp. 203–213.

[4] Shabrov, M. N., and Needleman, A., 2002, "An Analysis of Inclusion Morphology Effects on Void Nucleation," Modell. Simul. Mater. Sci. Eng., **10**, pp. 163–183.

[5] Needleman, A., 1990, "An Analysis of Decohesion Along an Imperfect Interface," Int. J. Fract., **42**, pp. 21–40.

[6] Needleman, A., 1990, "Analysis of Tensile Decohesion Along an Interface," J. Mech. Phys. Solids, **38**, pp. 289–324.

[7] Tvergaard, V., and Hutchinson, J. W., 1992, "The Relation Between Crack Growth and Fracture Process Parameters in Elastic-Plastic Solids," J. Mech. Phys. Solids, **40**, pp. 1377–1397.

[8] Xu, X. P., and Needleman, A., 1994, "Numerical Simulations of Fast Crack Growth in Brittle Solids," J. Mech. Phys. Solids, **42**, pp. 1397–1434.

[9] Pandolfi, A., Guduru, P. R., Ortiz, M., and Rosakis, A. J., 2000, "Three Dimensional Cohesive-Element Analysis and Experiments of Dynamic Fracture in C300 Steel," Int. J. Solids Struct., **37**(27), pp. 3733–3760.

[10] Ruiz, G., Pandolfi, A., and Ortiz, M., 2001, "Three-Dimensional Cohesive Modeling of Dynamic Mixed-Mode Fracture," Int. J. Numer. Methods Eng., **52**, pp. 97–120.

[11] Xu, X. P., and Needleman, A., 1995, "Numerical Simulations of Dynamic Interfacial Crack Growth Allowing for Crack Growth Away From the Bond Line," Int. J. Fract., **74**, pp. 253–275.

[12] Xu, X. P., and Needleman, A., 1996, "Numerical Simulations of Dynamic Crack Growth Along an Interface," Int. J. Fract., **74**, pp. 289–324.

[13] Siegmund, T., and Needleman, A., 1997, "A Numerical Study of Dynamic Crack Growth in Elastic-Viscoplastic Solids," Int. J. Solids Struct., **34**, pp. 769–787.

[14] Rosakis, A. J., Samudrala, O., Singh, R. P., and Shukla, A. 1998, "Intersonic Crack Propagation in Bimaterials," J. Mech. Phys. Solids-Special Volume on Dynamic Deformation and Failure Mechanics of Materials, 46, pp. 1789–1813.

[15] Camacho, G. T., and Ortiz, M., 1996, "Computational Modeling of Impact Damage in Brittle Materials," Int. J. Solids Struct., **33**, pp. 2899–2938.

[16] Miller, O., Freund, L. B., and Needleman, A., 1999, "Modeling and Simulation of Dynamic Fragmentation in Brittle Materials," Int. J. Fract., **96**(2), pp. 101–125.

[17] Espinosa, H., Zavattieri, P., and Emore, G., 1998, "A Finite Deformation Continuum/Discrete Model for the Description of Fragmentation and Damage in Brittle Materials," J. Mech. Phys. Solids, **46**(10), pp. 1909–1942.

[18] Espinosa, H., Zavattieri, P., and Emore, G., 1998, "Adaptive FEM Computation of Geometrical and Material Nonlinearities With Application to Brittle Materials," Mech. Mater., **29**, pp. 275–305.

[19] Zhai, J., and Zhou, M., 1998, "Micromechanical Modeling of Dynamic Fracture in Ceramic Composites," Special Technical Publication 1359 ASTM, pp. 174–200.

[20] Zhai, J., and Zhou, M., 1999, "Finite Element Analysis of Micromechanical Failure Modes in Heterogeneous Brittle Solids," Int. J. Fract. (special issue on Failure Mode Transition), pp. 161–180.

[21] Geubelle, P., and Baylor, J., 1998, "Impact-Induced Delamination of Compos-

ites: A 2D Simulation,'' Composites, Part B, **29**, pp. 589–602.

[22] Minnaar, K., and Zhou, M., 2000, "Real-Time Detection and Explicit Finite Element Simulation of Delamination in Composite Laminates Under Impact Loading,'' in *AMD ASME IMECE*, Orlando, FL, USA.

[23] Minnaar, K., and Zhou, M., 2001, "Experimental Characterization and Numerical Simulation of Impact Damage in Composite Laminates,'' in *ASME IMECE*, ASME NY.

[24] Espinosa, H. D., Dwivedi, S., and Lu, H.-C., 2000, "Modeling Impact Induced Delamination of Woven Fibre Reinforced Composites With Contact/Cohesive Laws,'' Comput. Methods Appl. Mech. Eng., **183**, pp. 259–290.

[25] Zou, Z., Reid, S. R., and Li, S., 2003, "A Continuum Damage Model for Delaminations in Laminated Composites,'' J. Mech. Phys. Solids, **51**, pp. 333–356.

[26] Xuan, W., Curtin, W. A., and Needleman, A., 2003, "Stochastic Microcrack Nucleation in Lamellar Solids,'' Eng. Fract. Mech., **70**, pp. 1869–1884.

[27] Rahul-Kumar, P., Jagota, A., Bennison, S. J., Saigal, S., and Muralidhar, S., 1999, "Polymer Interfacial Fracture Simulations Using Cohesive Elements,'' Acta Mater., **47**(15–16), pp. 4161–4169.

[28] Rahul-Kumar, P., Jagota, A., Bennison, S. J., Saigal, S., and Muralidhar, S., 2000, "Cohesive Element Modeling of Viscoelastic Fracture: Application to Peel Testing of Polymers,'' Int. J. Solids Struct., **37**(13), pp. 1873–1897.

[29] Rahul-Kumar, P., Jagota, A., Bennison, S. J., Saigal, S., and Muralidhar, S., 2000, "Interfacial Failures in a Compressive Shear Strength Test of Glass/Polymer Laminates,'' Int. J. Solids Struct., **37**(48–50), pp. 7281–7305.

[30] Roychowdhury, S., Arun Roy, Y. D., Dodds, J., and Robert, H., 2002, "Ductile Tearing in Thin Aluminum Panels: Experiments and Analyses Using Large-Displacement, 3-D Surface Cohesive Elements,'' Eng. Fract. Mech., **69**(8), pp. 983–1002.

[31] Zavattieri, P. D., Raghuram, P. V., and Espinosa, H. D., 2001, "A Computational Model of Ceramic Microstructures Subjected to Multi-Axial Dynamic Loading,'' J. Mech. Phys. Solids, **49**, pp. 27–68.

[32] Scheider, I., and Brocks, W., 2003, "Simulation of Cup-Cone Fracture Using the Cohesive Model,'' Eng. Fract. Mech., **70**, pp. 1943–1961.

[33] Gomez, F. J., and Elices, M., 2003, "Fracture of Components With V-Shaped Notches,'' Eng. Fract. Mech., **70**, pp. 1913–1927.

[34] Yuan, H., and Chen, J., 2003, "Computational Analysis of Thin Coating Layer Failure Using a Cohesive Model and Gradient Plasticity,'' Eng. Fract. Mech., **70**, pp. 1929–1942.

[35] Jin, Z.-H., Paulino, G. H., and Dodds, Jr., R. H., 2003, "Cohesive Fracture Modeling of Elastic-Plastic Crack Growth in Functionally Graded Materials,'' Eng. Fract. Mech., **70**, pp. 1885–1912.

[36] Carpinteri, A., Cornetti, P., Barpi, F., and Valente, S., 2003, "Cohesive Crack Model Crack Description of Ductile to Brittle Size-Scale Transition: Dimensional Analysis Versus Renormalization Group Theory,'' Eng. Fract. Mech., **70**, pp. 1809–1839.

[37] Pandolfi, A., Yu, C., Corigliano, A., and Ortiz, M., 1997, "Modeling Dynamic Fracture in Transversely Isotropic Composites: A Cohesive Approach,'' California Inbstitute of Technology, caltechASCI/2000.097.

[38] Yu, C., 2001, "Three-Dimensional Cohesive Modelling of Impact Damage of Composites,'' Ph.D. Thesis, Caltech, Pasadena, CA.

[39] Pandolfi, A., and Ortiz, M., 2002, "An Efficient Adaptive Procedure for Three-Dimensional Fragmentation Simulations,'' Eng. Comput., **18**, pp. 148–159.

[40] Spearot, D. E., Jacob, K. I., and McDowell, D. L., 2004, "Nonlocal Separation Constitutive Laws for Interfaces and Their Relation to Nanoscale Simulations,'' to appear in Mech. Mater.

[41] Falk, M. A., Needleman, A., and Rice, J. R., 2001, "A Critical Evaluation of Dynamic Fracture Simulations Using Cohesive Surfaces,'' in *Fifth European Mechanics of Material Conference*, Delft, The Netherlands.

[42] Papoulia, K. D., and Vavasis, S. A., 2002, "Time-Continuous Cohesive Interface Finite Elements in Explicit Dynamics,'' in *15th ASCE Engineering Mechanics Conference*, Columbia University, New York, NY.

[43] Prado, E. P., and van Mier, J. G. M., 2003, "Effect of Particle Structure on Model-I Fracture Process in Concrete,'' Eng. Fract. Mech., **70**, pp. 1793–1807.

[44] Sorensen, B. F., and Jacobsen, T. K., 2003, "Determination of Cohesive Laws by the J Integral Approach,'' Eng. Fract. Mech., **70**, pp. 1841–1858.

[45] Nguyen, O., and Ortiz, M., 2002, "Coarse-Graining and Renormalization of Atomistic Binding Relations and Universal Macroscopic Cohesive Behavior,'' J. Mech. Phys. Solids, **50**(8), pp. 1727–1741.

[46] Klein, P., Foulk, J., Chen, E., Wimmer, S., and Gao, H., 2000, "Physics-Based Modeling of Brittle Fracture: Cohesive Formulations and the Application of Meshfree Methods,'' SAND2001-8099, Sandia National Laboratories, USA.

[47] Logan, K. V., 1996, "Composite Ceramics, Final Tehnical Report,'' USSTACOM DAAEO7-95-C-R040.

[48] Ortiz, M., and Pandolfi, A., 1999, "Finite Deformation Irreversible Cohesive Elements for Three-Dimensional Crack-Propagation Analysis,'' Int. J. Numer. Methods Eng., **44**(9), pp. 1267–1282.

[49] Shet, C., and Chandra, N., 2002, "Analysis of Energy Balance When Using Cohesive Zone Models to Simulate Fracture Processes,'' J. Eng. Mater. Technol., **124**, pp. 440–450.

[50] Lin, Y. K., 1967, Probabilistic Theory of Structural Dynamics, McGraw-Hill.

[51] Nguyen, O., Repetto, E. A., Ortiz, M., and Radovitzky, R. A., 2001, "A Cohesive Model of Fatigue Crack Growth,'' Int. J. Fract., **110**, pp. 351–369.

[52] Krieg, R. D., and Key, S. W., 1973, "Transient Shell Response by Numerical Integration,'' Int. J. Numer. Methods Eng., **7**, pp. 273–286.

[53] Belytschko, T., Chiapetta, R. L., and Bartel, H. D., 1976, "Efficient Large Scale Non-Linear Transient Analysis by Finite Elements,'' Int. J. Numer. Methods Eng., **10**, pp. 579–596.

[54] Tomar, V., and Zhou, M., 2004, "Deterministic and Stochastic Analyses of Dynamic Fracture in Two-Phase Ceramic Microstructures With Random Material Properties,'' manuscript in preparation.

[55] Tomar, V., and Zhou, M., 2004, "Deterministic and Stochastic Analyses of Fracture Processes,'' in *International Conference on Heterogeneous Material Mechanics*, Chongqing University, China.

[56] Johnson, E., 1992, "Process Region Changes for Rapidly Propagating Cracks,'' Int. J. Fract., **55**, pp. 47–63.

[57] Ravi-Chandar, K., and Knauss, W. G., 1984, "An Experimental Investigation Into Dynamic Fracture-I. Crack Initiation and Arrest,'' Int. J. Fract., **25**, pp. 247–262.

[58] Ravi-Chandar, K., and Knauss, W. G., 1984, "An Experimental Investigation Into Dynamic Fracture II. Microstructural Aspects,'' Int. J. Fract., **26**, pp. 65–80.

[59] Ravi-Chandar, K., and Knauss, W. G., 1984, "An Experimental Investigation Into Dynamic Fracture III. Steady-State Crack Propagation and Crack Branching,'' Int. J. Fract., **26**, pp. 141–154.

[60] Ravi-Chandar, K., and Knauss, W. G., 1984, "An Experimental Investigation Into Dynamic Fracture IV. On the Interaction of Stress Waves With Propagating Cracks,'' Int. J. Fract., **26**, pp. 192–203.

[61] Keller, A. R., and Zhou, M., 2003, "Effect of Microstructure on Dynamic Failure Resistance of TiB2/Al2O3 Ceramics,'' J. Am. Ceram. Soc., **86**(3), pp. 449–57.